SUB | NIEDERSÄCHSISCHE STAATS- UND UNIVERSITÄTSBIBLIOTHEK GÖTTINGEN

Werk

Jahr: 1981
Kollektion: fid.geo
Signatur: 8 Z NAT 2148:49
Digitalisiert: Niedersächsische Staats- und Universitätsbibliothek Göttingen
Werk Id: PPN1015067948_0049
PURL: http://resolver.sub.uni-goettingen.de/purl?PPN1015067948_0049

LOG Id: LOG_0024
LOG Titel: Application of different methods for the determination of ionospheric conductivities from sounding rocket observations
LOG Typ: article

Übergeordnetes Werk

Werk Id: PPN1015067948
PURL: http://resolver.sub.uni-goettingen.de/purl?PPN1015067948
OPAC: http://opac.sub.uni-goettingen.de/DB=1/PPN?PPN=1015067948

Terms and Conditions

The Goettingen State and University Library provides access to digitized documents strictly for noncommercial educational, research and private purposes and makes no warranty with regard to their use for other purposes. Some of our collections are protected by copyright. Publication and/or broadcast in any form (including electronic) requires prior written permission from the Goettingen State- and University Library.
Each copy of any part of this document must contain there Terms and Conditions. With the usage of the library's online system to access or download a digitized document you accept the Terms and Conditions.
Reproductions of material on the web site may not be made for or donated to other repositories, nor may be further reproduced without written permission from the Goettingen State- and University Library.

For reproduction requests and permissions, please contact us. If citing materials, please give proper attribution of the source.

Contact

Niedersächsische Staats- und Universitätsbibliothek Göttingen
Georg-August-Universität Göttingen
Platz der Göttinger Sieben 1
37073 Göttingen
Germany
Email: gdz@sub.uni-goettingen.de

J. Geophysik 49, 74–81 (1981)

Journal of Geophysics

Application of Different Methods for the Determination of Ionospheric Conductivities from Sounding Rocket Observations

K. Brüning [1], W. Baumjohann [1], K. Wilhelm [2], W Stüdemann [2], A. Urban [3], W Ott [4], K. Spenner [4], G.L. Schmidtke [5], and H.M. Fischer [5]

[1] Institut für Geophysik der Universität Münster, Gievenbecker Weg 61, D-4400 Münster, Federal Republic of Germany
[2] Max-Planck-Institut für Aeronomie, D-3411 Katlenburg-Lindau 3, Federal Republic of Germany
[3] Institut für Weltraumforschung der Österreichischen Akademie der Wissenschaften, A-8010 Graz, Austria
[4] Fraunhofer Institut für Physikalische Meßtechnik, D-7800 Freiburg, Federal Republic of Germany
[5] Institut für Reine und Angewandte Kernphysik der Universität Kiel, D-2300 Kiel, Federal Republic of Germany

Abstract. On 2 November 1977, at 2015 UT, the sounding rocket payload F1B of the 'Substorm Phenomena' campaign was launched from Andenes (Norway). The rocket flew approximately northwards and traversed first an area of weak and diffuse auroral forms in the Harang discontinuity region and then an auroral arc in the region of the westward electrojet. From the particle measurements obtained during the flight ionospheric conductivities are calculated using two different methods. When the classical method is used, i.e., height-integrated conductivities are calculated from the measured thermal electron densities and temperatures, only two values can be determined which are temporally and spatially averaged over the upleg and downleg part of the trajectory, respectively. The calculation of height-integrated conductivities from the measured energetic electron spectra, on the other hand, yields instantaneous values for every location where a spectrum has been sampled. Since there were substantial fluxes of energetic protons during the flight F1B, we also take those into account. The height-integrated conductivities calculated with the two different methods for closely neighbouring regions and the same geophysical situation are nearly identical. A comparison between the contributions of energetic electrons and protons shows that, above 130 km altitude, the ionization rates of the incident protons were higher than those of the electrons while below this altitude the ionization caused by the incident electrons prevailed. Hence, most of the ionospheric conductivity above 130 km was created by energetic protons while below 130 km altitude the energetic electron contribution was dominant.

Key words: Auroral zone – Ionization – Electron density – Conductivities – Energetic electrons – Energetic protons.

Introduction

Ionospheric conductivities play an important role in the electrodynamics of the auroral oval. While the meridional and even two-dimensional distributions of other important parameters like magnetic and electric fields are already rather well known (Baumjohann et al. 1980, and references therein), the spatial and temporal variations of the ionospheric Hall and Pedersen conductivities are still relatively unexplored. They may be calculated for a particular location and moment of time if the instantaneous vertical (along a magnetic flux tube) altitude profile of the electron density (N_e) between 90 and about 200 km is known.

In general, there are two different methods for the determination of N_e altitude profiles in the auroral zone. The first is based on relatively direct measurements of the thermal electrons by incoherent scatter and rocket borne plasma analyzers. Vertical and nearly instantaneous N_e altitude profiles have been measured with the Chatanika incoherent scatter radar (e.g. Brekke et al. 1974; Banks and Doupnik 1975), but the measurements were restricted to only a few locations in the auroral ionosphere. Altitude profiles of N_e have also been measured during rocket flights (e.g. Primdahl et al. 1979) but the profiles were neither vertical nor instantaneous. Hence, the authors could give only two values for the height-integrated conductivity, one for the upleg and one for the downleg part of the rocket trajectory. These values were only approximate values, since the height-integration of the conductivities was not made along flux tubes of homogeneous energy deposition but along the rocket trajectory and was thus dependent on the temporal and spatial variability of the energy deposition along the trajectory.

The second method is based on measurements of the energy spectra of precipitating energetic particles. Here, the ionization caused by the incident energetic electrons and protons is computed using the methods given by Rees (1963) and Eather and Burrows (1966), respectively. By assuming reasonable values for the recombination coefficients, vertical and instantaneous altitude profiles of N_e may be calculated for every flux tube where a spectrum has been sampled. Hence, height-integrated conductivities may be calculated nearly everywhere along the whole rocket trajectory, provided that electron and proton spectra cover a sufficiently broad energy range and have been sampled high enough above the absorbing layers of the ionosphere.

The second method has already been used by several authors (Sharp et al. 1975; Rees et al. 1976; Evans et al. 1977; Behm et al. 1979). In all these studies the ionization caused by incident energetic electrons alone was considered, since the incident proton fluxes were either weak or not measured. However, by comparing the ionization efficiencies of energetic electrons given by Rees (1963; his Fig. 2) with those of energetic protons given by Eather and Burrows (1966; their Fig. 5a) one may note that the ionization caused by incident energetic protons is not negligible if the proton fluxes are of the same order or slightly lower than the electron fluxes.

In the present study we shall calculate height-integrated conductivities using data from a sounding rocket payload which included a thermal plasma analyzer and several energetic electron

0340-062X/81/0049/0074/$01.60

Table 1. Experiments flown aboard the payload 'Substorm Phenomena F1B' and used in this study

Experiment	Technique	Measurements	Institution
Plasma experiment TF 4	Retarding potential analyser	Electron temperature, ion density, ion wind, vehicle potential electron flux 0–30 eV	IPM, Freiburg
Particle spectrometer Electrons TL 7 Protons TZ 1	Hemispherical electrostatic analyser and open electron multipliers	Electron and proton fluxes $0.1(1) \leqq E_e(E_p) \leqq 25(40)$keV	MPAE, Lindau INW, Graz
Particle spectrometer TL 6	Magnetic particle analyser and solid-state detectors	Electron and proton fluxes $20(40) \leqq E_e(E_p) \leqq 200(300)$keV	MPAE, Lindau
Particle spectrometer TK 1	Solid-state detector telescope	Proton fluxes $0.07 \leqq E_p \leqq 2$ MeV	IFKKI, Kiel

and proton detectors. This extensive data suite enables us to apply both methods and, for the first time, to include the energetic proton contribution when using the second method. Where possible, we shall compare the values given by the two different methods and in particular, we shall discuss the relevance of energetic proton fluxes in creating ionospheric conductivities.

Instrumentation

The payload F1B was integrated as part of a larger sounding rocket programme named 'Substorm Phenomena'. The experiment complements were selected to provide a set of plasma, particle and field observations during various phases of magnetospheric substorm events. Details of the experiments used in this study are compiled in Table 1, which also indicates the various institutions responsible for the particular instrument developments.

The payloads were launched by Skylark 12 motors from the Andøya rocket range, Norway, and flight F1B, which was launched on 2 November 1977 at 2015 UT, lasted for about 12 min and reached a peak altitude of 542.4 km. The payload was controlled in attitude so as to point $20° \pm 10°$ off the negative geomagnetic field direction and had a spin period of 350 ms. The trace of the rocket trajectory is shown in Fig. 1, at a height of 100 km (projected down along magnetic field lines).

Geophysical Situation During Flight

In order to establish the configuration of the electrojet and the optical aurora during the rocket flight, data from the Scandinavian Magnetometer Array (SMA; Küppers et al. 1979; Maurer and Theile 1978) and from the all-sky camera at Abisko (Sweden) have been analysed.

In Fig. 1 the equivalent current arrows on the Earth's surface and the location of an auroral arc are displayed for 2020 UT, the most relevant interval. The coordinate system indicated in Fig. 1 has been introduced by Küppers et al. (1979) and named the Kiruna system. It is a Cartesian system obtained by a projection of the globe onto a tangential plane centered at Kiruna, Sweden (67.8°N, 20.4°E). The y_{KI} axis of the system has been chosen as the tangent to the projection of the ϕ_c (KIR) = 64.8° line with ϕ_c being the revised corrected geomagnetic latitude as given by Gustafsson (1970). The x_{KI} axis is perpendicular to the y_{KI} axis and is directed approximately 12° west of geographic north at Kiruna, where the system has its origin ($x_{KI} = y_{KI} = 0$).

The SMA observations (Fig. 1) indicate that between 2000 and 2030 UT (i.e., 1 h before magnetic midnight) Scandinavia was

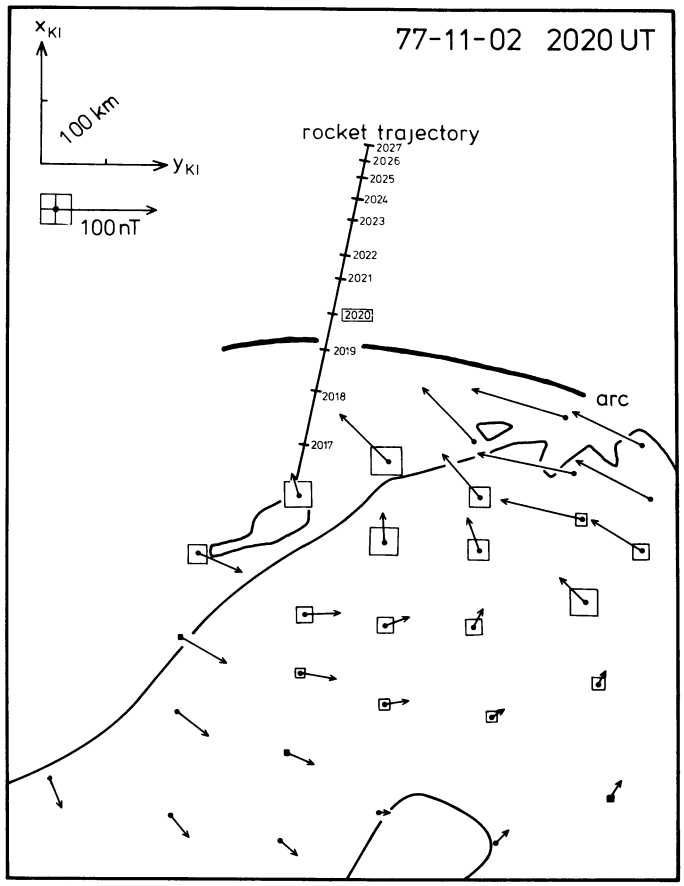

Fig. 1. Equivalent current arrows on the Earth's surface. The *current arrows* have their origin at the station, where the corresponding magnetic disturbances have been observed. The *squares* denote negative Z components. The position of the auroral arc and the rocket trajectory have been added

situated under the Harang discontinuity region (Harang 1946; Heppner 1972; see Baumjohann et al. 1980, for SMA signatures of the Harang discontinuity) and both SMA and all-sky camera data show the signatures of substorm activity. After the passage of a westward travelling surge around 2000 UT the aurora intensified again and after 2010 UT formed a large spiral which broke up at 2013 UT. Later, the aurora became weaker and more diffuse in the south. At the northern boundary of auroral activity a single arc formed which was located north of the Norwegian coast at 2020 UT (see Fig. 1). This arc intensified again at 2026 UT leading

to another breakup at 2028 UT. Each of the auroral intensifications was accompanied by a strong enhancement of the westward electrojet. A compilation of additional observations relevant to this event has been given elsewhere (Wilhelm 1980).

In summary, the payload F1B traversed an area of diffuse auroral forms near the Harang discontinuity shortly after the launch. Between 235 and 275 s after launch it traversed an auroral arc located in the westward electrojet region.

Calculation of Ionospheric Conductivities from Measured Electron Density and Temperature Profiles

Using suitable models for the neutral atmospheric densities, it is possible to compute ionospheric electrical conductivities from measured electron density (N_e) and temperature (T_e) profiles. The altitude dependent Hall (σ_H) and Pedersen (σ_P) conductivities are defined by the well-known expressions (neglecting ion-electron collisions):

$$\sigma_H = \frac{N_e e}{B}\left(\frac{\omega_e^2}{\omega_e^2+\nu_e^2}-\frac{\omega_i^2}{\omega_i^2+\nu_i^2}\right)$$
$$\sigma_P = \frac{N_e e}{B}\left(\frac{\omega_e \nu_e}{\omega_e^2+\nu_e^2}+\frac{\omega_i \nu_i}{\omega_i^2+\nu_i^2}\right) \quad (1)$$

where e is the electron charge, B is the magnetic field magnitude, $\omega_{i,e}=eB/m_{i,e}$ is the ion (or electron) gyrofrequency, $m_{i,e}$ is the ion (or electron) mass and $\nu_{i,e}$ is the ion (or electron) neutral collision frequency. The collision frequencies may be calculated as follows (note that only T_e was measured and thus a T_i-independent expression for ν_i has to be used):

$$\nu_e = 1.5\times 10^{-17}\, M\, T_e$$
$$\nu_i = 4.2\times 10^{-16}\, M \quad (2)$$

where M is the number of neutrals (Boström 1973; Jones and Rees 1973).

The N_e and T_e profiles which have been measured by a retarding potential analyzer (plasma experiment TF4; see Table 1) during the flight F1B are displayed in Figs. 2 and 3. In both figures a pronounced difference between the upleg and downleg profiles can be noted. These differences can be explained by the fact that the payload entered regions with different auroral activity and probably left the auroral oval at about 660 s after launch (2026 UT). At this moment, the electron fluxes observed by the spectrometer TL7 (see Table 1) fell below the instrument threshold, supporting the assumption of polar cap conditions after 2026 UT, since in the polar cap only electrons below 1 keV precipitate (polar rain, Winningham et al. 1975; Heelis et al. in press 1980). Such electrons do not reach altitudes below 150 km (Rees 1963), a fact that may explain the extremely low electron densities after 2026 UT and below 200 km altitude.

The minima and maxima in the upleg T_e profile are related to strong spatial and partially also to temporal variations of the ionospheric conditions. A comparison with the all-sky camera photographs reveals that the rocket traversed a diffuse auroral patch near 2016 UT and was located between this patch and an auroral arc after 2017 UT. Hence, the T_e maximum between 75 and 100 s after launch is probably related to the auroral patch, while the high electron temperatures around 250 s after launch (2019–2929 UT) coincide with the auroral arc crossing (Fig. 1). Also plotted in Fig. 3 is a model T_e profile as given by Jones and

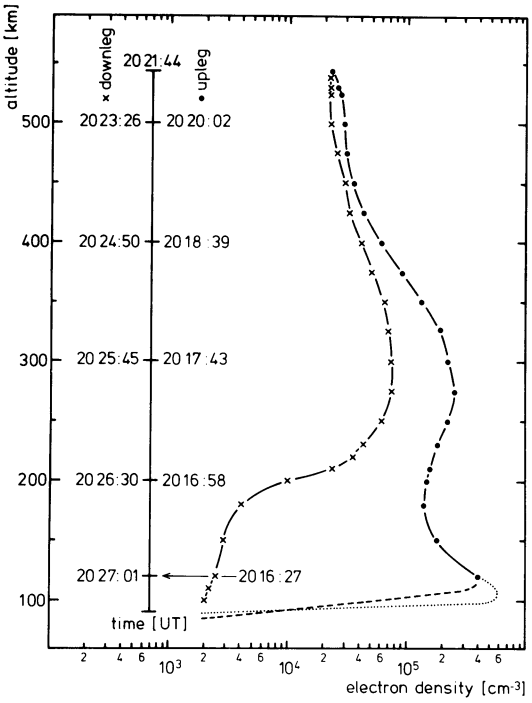

Fig. 2. Altitude profiles of electron density measured during the upleg and downleg part of flight F1B. *Dotted* and *dashed lines* give possible extrapolations of the upleg curve (for details see text)

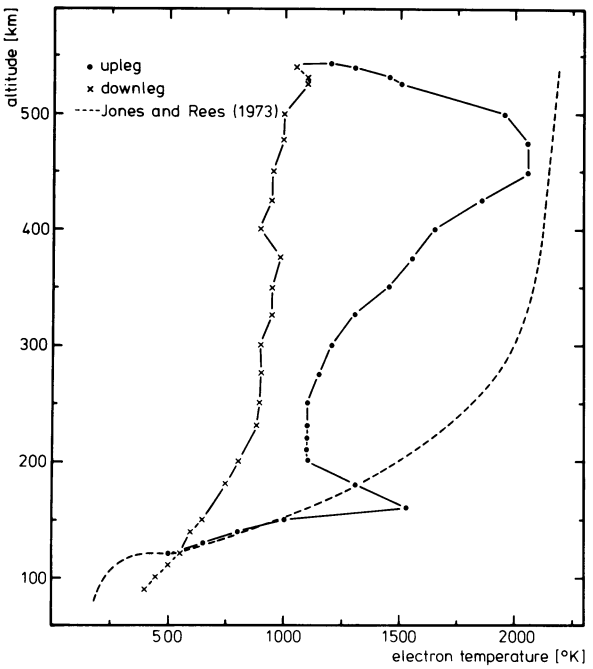

Fig. 3. Altitude profiles of electron temperature measured during the upleg and downleg part of flight F1B. For comparison the model curve of Jones and Rees (1973) has been added

Rees (1973) for the night-time auroral zone. The significant difference between this profile and the measured ones indicates that one has to be careful in using model T_e profiles for estimating ν_e in Eq. (2). Model T_e values must nevertheless be used in this study for the upleg profile below 120 km, since no T_e measurements

were possible during this part of the flight (before the third stage burned out).

Similarly the electron density could not be measured below 120 km on the upleg profile. Hence, we had to assume N_e values between 90 and 120 km. Two possibilities are indicated in Fig. 2. The dashed curve was drawn with the assumption that the measured electron density at 120 km is the maximum value (a) while the dotted line represents an increase of N_e below 120 km to a maximum of 6×10^5 electrons/cm^3 at 105 km altitude (b). Justification for the latter extrapolation (b) may be found in the fact that similar values have been measured by the Chatanika incoherent scatter radar for disturbed times (Baron 1972) and in the N_e values calculated by the second method for a neighbouring region (Fig. 7).

The height-integrated (90–400 km) Hall and Pedersen conductivities calculated from the profiles in Figs. 2 and 3 are as follows:

upleg:

(a) $\Sigma_H = 23$ mho, $\Sigma_P = 15$ mho, $\frac{\Sigma_H}{\Sigma_P} = 1.5$

(b) $\Sigma_H = 46$ mho, $\Sigma_P = 17$ mho, $\frac{\Sigma_H}{\Sigma_P} = 2.7$

downleg:

$\Sigma_H = 0.2$ mho, $\Sigma_P = 0.2$ mho, $\frac{\Sigma_H}{\Sigma_P} = 1.0$

The height-integrated conductivities and their ratio during the upleg part of the trajectory are within the range of values given by other authors for similar auroral conditions (Brekke et al. 1974; Wedde et al. 1977; Horwitz et al. 1978a, b). Since Σ_H depends strongly on the electron densities between 90 and 120 km, where the plasma parameters could not be measured, the calculated values give only an order of magnitude. The calculated value for Σ_P is more reliable since σ_P has its maximum at higher altitudes and only 15% of the total contribution to Σ_P is influenced by the uncertainty in N_e between 90 and 120 km. Of course, additional errors could be introduced by temporal and spatial fluctuations. However, about 70% of the total height-integrated Pedersen conductivity stems from contributions of σ_P between 120 and 150 km. The rocket flew through this altitude range within 15 s covering a horizontal distance of 15 km. Accordingly $\Sigma_P = 16 \pm 8$ mho seems to be a representative value for the time 2016:30 UT and the location $x_{KI} \approx 250$ km.

The Hall and Pedersen conductivities calculated from the downleg N_e and T_e profiles are extremely small. This is mainly caused by the very low electron density measured in the *E*-layer. In line with the above arguments, the height-integrated conductivities given are probably representative for the polar cap region.

Since the payload traversed regions with quite different ionospheric conditions, the height-integrated conductivities along the trajectory are by no means constant and the method described yields useful information only in areas where the payload was within or close to the *E*-layer. For a more exact calculation of the height-integrated conductivities along the trajectory, we need, at least, instantaneous N_e profiles for a number of locations. These may be calculated by the method given in the next section.

Calculation of Ionospheric Conductivities from Measured Energetic Particle Spectra

Instantaneous N_e altitude profiles for numerous locations along the rocket trajectory may be calculated from the measured energetic particle spectra. This is done by computing altitude profiles of the ionization rate $q(h)$ due to the measured precipitating energetic particles with the methods given by Rees (1963), Eather and Burrows (1966), and Eather (1970). Below 200 km the N_e profile is then given by (Rishbeth and Garriott 1969)

$$N_e(h) = \sqrt{\frac{q(h)}{\alpha(h)}} \tag{3}$$

where $\alpha(h)$ is the altitude dependent recombination coefficient (we use the values given by Evans et al. 1977). When substituting these instantaneous N_e profiles into Eq. (1) instantaneous and vertical σ_H and σ_P altitude profiles can be obtained.

As already indicated, our study goes further than earlier ones in that we incorporate the contribution of energetic protons to

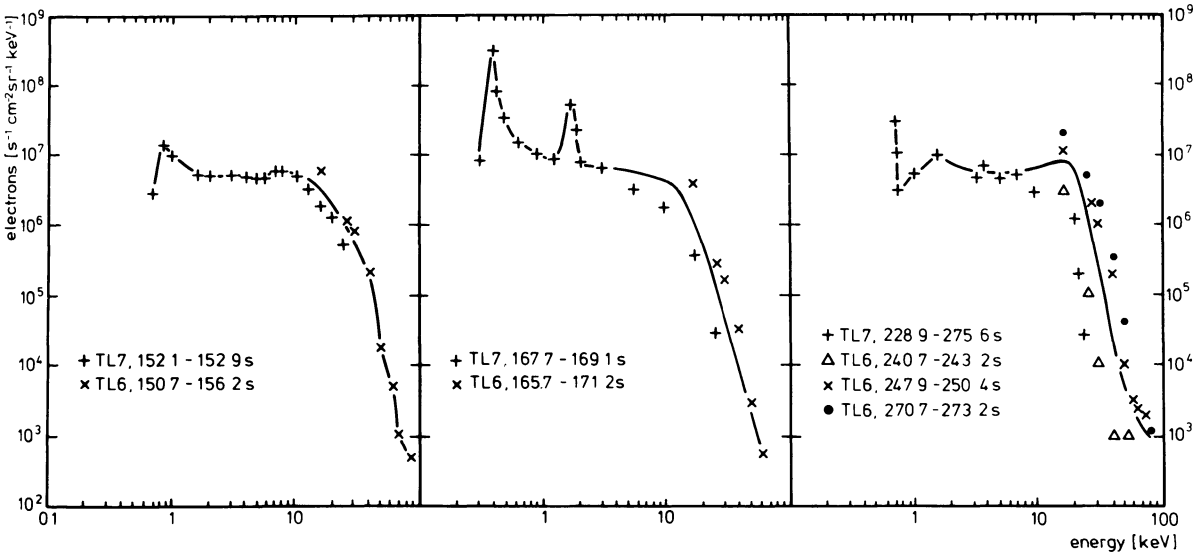

Fig. 4. Representative electron spectra constructed from measurements of the experiments TL6 and TL7. The *left* and *middle spectra* have been measured when the rocket traversed diffuse auroral forms near the Harang discontinuity. The *right spectrum* was measured when the rocket crossed an auroral arc

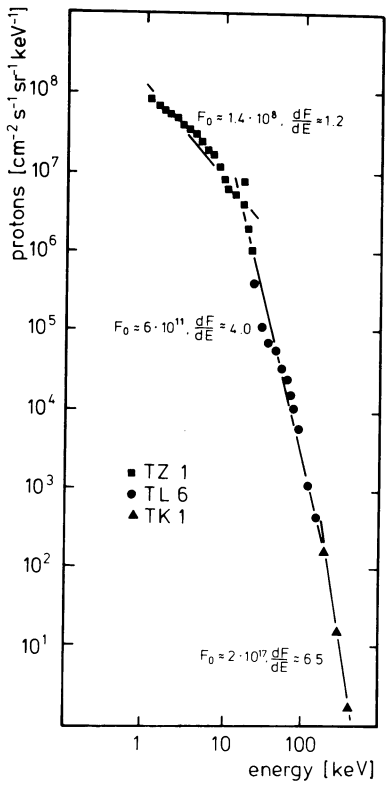

Fig. 5. Representative proton spectrum constructed from measurements of the experiments *TZ*1, *TL*6, and *TK*1 made around 125 s after launch

the ionization rates. We have also gone further than earlier studies by combining spectra measured by particle spectrometers covering adjacent energy ranges (TL7 and TL6 for electrons; TZ1, TL6, and TK1 for protons; see Table 1) in order to determine the contributions from particles in a wider energy range (0.4–100 keV for electrons and 1–400 keV for protons as compared to the maximum 16 keV used by Evans et al. 1977). This is important since high-energy particles penetrate deeper into the ionosphere (especially into the lower *E*-layer) and ionize more neutral particles. Their small number densities compared to particles with energies below, say, 20 keV can thus be partially balanced by their greater efficiency in creating ionization.

Experiment TL7 measured electron spectra at 152–215 s and 357–442 s after launch with a short sweep time of 1.4 s while at 229–352 s the scan time was 46.7 s. Experiment TL6 measured electron spectra every 0.6 s at 106–280 s after launch, which were integrated over times of 2.5 and 5.5 s. For those times shown in Fig. 4 spectra of both experiments are combined. The pitch angle distributions (not shown here) were also determined and helped to decide whether isotropic ($<80°$) or cosine-dependent particle distributions had to be used in Rees' algorithm.

The proton spectra are combined from the data obtained by the experiments TZ1, TL6, and TK1 for the interval 100–340 s. Each of the spectra can be represented by power law functions in the energy ranges 1–20, 20–200, and 200–400 keV. An example is given in Fig. 5 for a time of 125 s after launch. For intervals in which the spectral indices and parameters are rather similar, we use average spectra. Although the observed proton fluxes were anisotropic (field-aligned), we decided to employ the ionization rates given by Eather and Burrows (1966) for isotropic distributions only. The proton flux measured at 20° pitch angle was taken to be representative in the interval 0°–60°.

In the following we shall use (average) spectra sampled at 150–300 s after launch. During this interval the payload flew at altitudes above 400 km. Hence, we can assume that the fraction of energy already deposited by the incident energetic particles is negligible and that there are hardly any neutral hydrogen atoms to cause spreading of the proton beam (Eather 1967).

In order to show that the number of precipitating energetic protons is indeed high enough to ionize a significant number of neutrals, we compare the integral particle fluxes for energetic electrons and protons (in the energy range 1–100 keV) in Fig. 6. It is apparent that during the flight F1B the integral proton flux was unusually strong and always higher than the electron flux. This is especially significant immediately south of the auroral arc where the electron fluxes were even below the instrument threshold. Only when the payload traversed the auroral arc around 250 s after launch and at about $x_{KI}=450$ km, were the flux levels of electrons and protons nearly identical (about 10^9 particles/cm^2 s). Hence, one may conclude that to omit to consider the proton

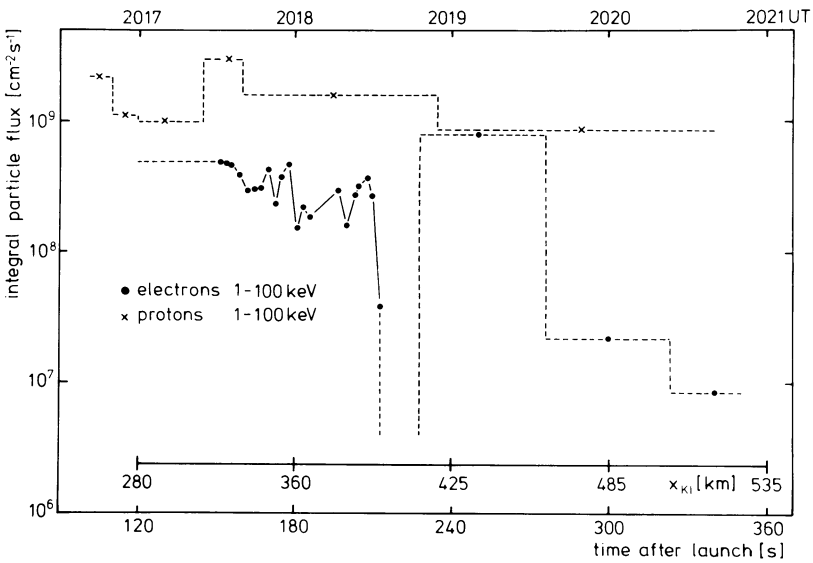

Fig. 6. Comparison of integral electron and proton fluxes (1–100 keV). The *dashed lines* represent averages while the *solid lines* connect values computed from high time-resolution spectra

contribution would lead to a serious underestimation of the ionization rates as well as the electron densities and thus the ionospheric conductivities.

For a more detailed analysis of the influence of electrons and protons on the altitude profiles of ionization rate, electron density and Hall and Pedersen conductivities, we calculate those values from the electron and proton spectra measured near 152 s after launch (the electron spectrum is shown in the left panel of Fig. 4 while the proton spectrum was similar to that displayed in Fig. 5). The results are displayed in Figs. 7 and 8. It can easily be seen that the ionization rate and the electron density below 110 km are dominated by the energetic electron contribution, while above this altitude the energetic proton contribution prevails. The different altitude dependence can be explained by the fact that the mean free path for energetic protons is smaller than that of electrons having the same energy and hence, on the average, the protons do not penetrate so deeply into the lower ionosphere. The altitude dependence is also reflected in the Hall and Pedersen conductivity profiles: the Pedersen conductivity with its maximum at 130 km is caused mainly by incident energetic protons while the Hall conductivity which has its maximum at 100 km height, is dominated by the energetic electron contribution.

The same tendency can also be seen in Fig. 9 where we display the height-integrated Hall and Pedersen conductivities and their ratio along the rocket trajectory and compare the values calculated from $q_e(h)$ only (left diagram) and from $q(h)=q_e(h)+q_p(h)$ (right diagram). This comparison shows that for flight F1B the ionization by energetic protons cannot be neglected. In particular, both to the south (215–230 s after launch) and north (> 280 s) of the auroral arc the height-integrated conductivities are caused mainly by energetic proton fluxes, which were about 100 times more intense than the electron fluxes at these locations (Fig. 6). In these areas,

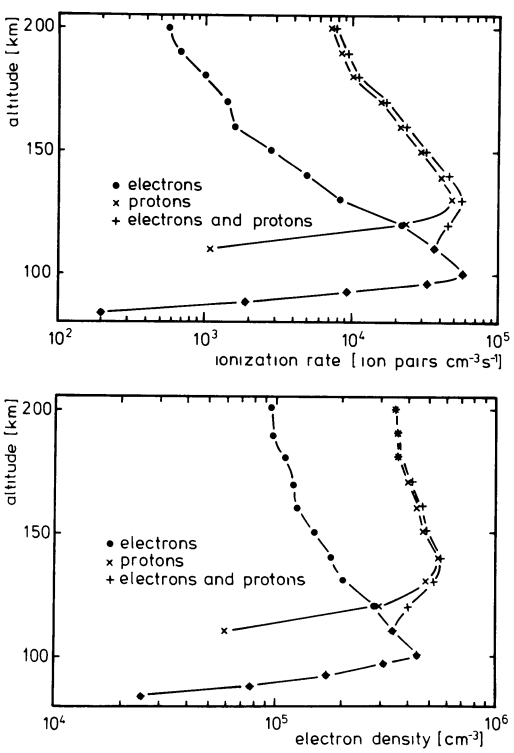

Fig. 7. Altitude profiles of total ionization rates (*upper panel*) and electron densities (*lower panel*) around 152 s after launch. Also given are curves representing the contributions of electrons and protons separately

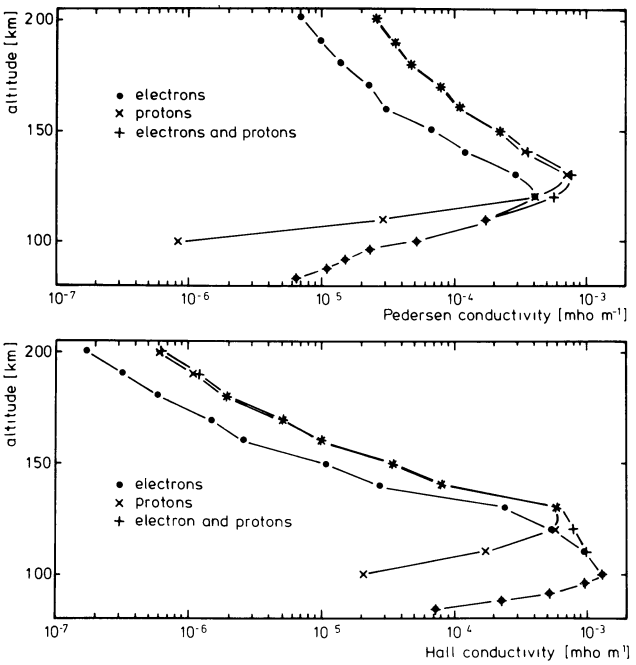

Fig. 8. Altitude profiles of Pedersen (*upper panel*) and Hall (*lower panel*) conductivities calculated from the electron density profiles given in Fig. 7

the height-integrated Hall conductivity is also mainly due to protons, while otherwise the energetic protons contribute mainly to the height-integrated Pedersen conductivity, as already shown in Fig. 8. The fact that about one half of the height-integrated Pedersen conductivity, but only about 20% of the height-integrated Hall conductivity, is caused by protons is also reflected in the Σ_H/Σ_P ratios (lower panels in Fig. 9). They range between 1 and 3 when considering precipitating electrons only and between 1 and 2 when the additional effects of precipitating protons are taken into account.

When considering the height-integrated conductivities and their ratio in relation to the optical aurora and the electrojets (see above) it seems noteworthy that in the Harang discontinuity, where diffuse auroral forms have been observed, the calculated values ($\Sigma_H=40$ mho, $\Sigma_P=20$ mho) are slightly higher than those given by Horwitz et al. (1978a). The values calculated for times when the rocket traversed the auroral arc within the westward electrojet ($\Sigma_H=48$ mho, $\Sigma_P=22$ mho) are comparable to those given by Evans et al. (1977) and Horwitz et al. (1978a). Finally, it seems interesting that the Σ_H/Σ_P ratio is always close to 2 in regions where aurora has been observed and close to 1 outside these regions (south and north of the arc).

Summary and Conclusions

In Table 2 we summarize the calculated height-integrated conductivities and their ratio in different latitudinal regions of the high-latitude ionosphere. The values in the first and last row are calculated from the measured N_e and T_e profiles (method 1 above) while the other four are calculated from the energetic particle spectra (method 2 above). It is apparent that there are strong variations of the height-integrated conductivities along the rocket trajectory which can only be resolved when using the second method. Since additional atmospheric model parameters (e.g., recombination

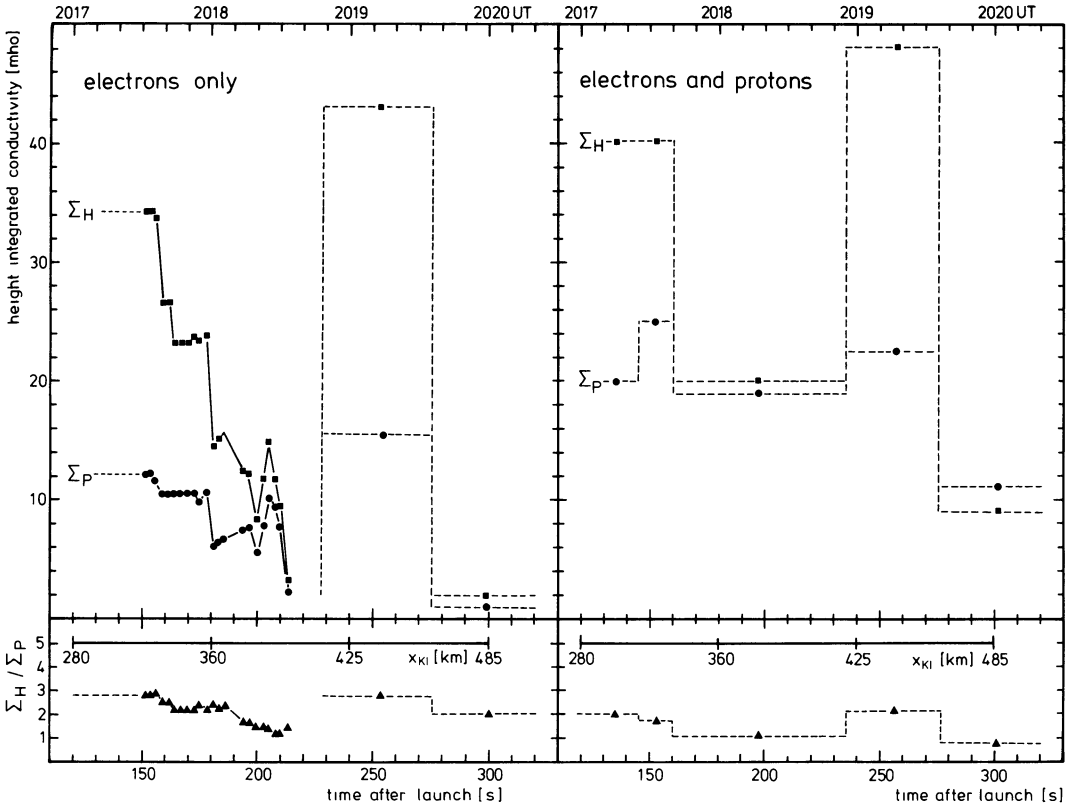

Fig. 9. Height-integrated conductivities and Σ_H/Σ_P ratio along a part of the rocket trajectory. The values in the left diagram are calculated from the electron spectra only, while in the right diagram electron and proton contributions are taken into account

Table 2. Average conductivities for the different regions traversed by the rocket

x_{KI} [km]	Aurora	Electrojet	Σ_H [mho]	Σ_P [mho]	Σ_H/Σ_P	Method used
~250	Diffuse auroral forms	Harang discontinuity	~35	16	~2	1
280–330	Diffuse auroral forms	Harang discontinuity	40	22	1.8	2
330–420	No aurora	Westward electrojet	20	19	1.1	2
420–460	Auroral arc	Westward electrojet	48	22	2.2	2
460–500	No aurora	Westward electrojet?	9	11	0.8	2
~700	No aurora	Polar cap?	0.2	0.2	1.0	1

coefficients) have to be used for the electron density calculations in method 2, it is probably less accurate than method 1. However, a comparison of the values given in the first two rows of Table 2, which are representative of closely neighbouring regions and the same geophysical conditions but are calculated by the two different methods, shows that both methods yield nearly the same results. A comparison of these values with the corresponding ones in the left diagram of Fig. 9 shows that a neglect of the energetic proton contribution in method 2 results in an under-estimation of the conductivities and the height-integrated Pedersen conductivity in particular, at least for conditions with high proton fluxes.

Acknowledgements. Many individuals at various institutions contributed to this sounding rocket programme. In particular, we should like to mention J. Hörle as project manager of DFVLR-PT. We also want to thank the integration team of Dornier System, the DFVLR launch team and the personnel of the Andøya Rocket Range for their support of the project. The work was supported financially by the German Bundesministerium für Forschung und Technologie and by the Österreichische Akademie der Wissenschaften. The SMA observations were made in cooperation with various institutions (Küppers et al. 1979) and supported financially by the Deutsche Forschungsgemeinschaft. We are indebted to M.H. Rees and R.H. Eather for useful comments on an earlier version of the manuscript. Finally, we would like to thank H. Lauche for putting the all-sky camera pictures at our disposal and H. Maurer for the data from the Braunschweig magnetometer chain.

References

Banks, P.M., Doupnik, J.R.: A review of auroral zone electrodynamics deduced from incoherent scatter radar observations. J. Atmos. Terr. Phys. **37**, 951–972, 1975

Baron, M.J.: DNA Project 617 radar, final report: Auroral ionospheric measurements. Menlo Park, California: Stanford Res. Inst. 1972

Baumjohann, W., Untiedt, J., Greenwald, R.A.: Joint two-dimensional observations of ground magnetic and ionospheric electric fields associated with auroral zone currents. 1. Three-dimensional current

flows associated with a substorm-intensified eastward electrojet. J. Geophys. Res. **85**, 1963–1978, 1980

Behm, D.A., Primdahl, F., Zanetti, L.J. Jr., Arnold, R.L., Cahill, L.J.Jr.: Ionospheric electrical currents in the late evening plasma flow reversal. J. Geophys. Res. **84**, 5339–5343, 1979

Boström, R.: Electrodynamics of the ionosphere. In: Cosmical geophysics, A. Egeland et al., eds.: pp. 181–192. Oslo: Universitetsforlaget 1973

Brekke, A., Doupnik, J.R., Banks, P.M.: Incoherent scatter measurements of *E* region conductivities and currents in the auroral zone. J. Geophys. Res. **79**, 3773–3790, 1974

Eather, R.H.: Auroral proton precipitation and hydrogen emissions. Rev. Geophys. **5**, 207–285, 1967

Eather, R.H.: Ionization produced by auroral proton precipitation. Ann. Géophys. **26**, 609–613, 1970

Eather, R.H., Burrows, K.M.: Excitation and ionization by auroral protons. Aust. J. Phys. **19**, 309–322, 1966

Evans, D.S., Maynard, N.C., Trøim, J., Jacobsen, T., Egeland, A.: Auroral vector electric field and particle comparisons. 2. Electrodynamics of an arc. J. Geophys. Res. **82**, 2235–2249, 1977

Gustafsson, G.: A revised corrected geomagnetic coordinate system. Ark. Geofys. **5**, 595–617, 1970

Harang, L.: The mean field of disturbance of polar geomagnetic storms. Terr. Magn. Atmos. Electr. **51**, 353–380, 1946

Heelis, R.A., Winningham, J.D., Hanson, W.B., Burch, J.L.: The relationships between high latitude convection reversals and the energetic particle morphology observed by Atmosphere Explorer. J. Geophys. Res. in press 1980

Heppner, J.P.: The Harang discontinuity in auroral belt ionospheric currents. Geofys. Publ. **29**, 105–120, 1972

Horwitz, J.L., Doupnik, J.R., Banks, P.M.: Chatanika radar observations of the latitudinal distributions of auroral zone electric fields, conductivities, and currents. J. Geophys. Res. **83**, 1463–1481, 1978a

Horwitz, J.L., Doupnik, J.R., Banks, P.M., Kamide, Y., Akasofu, S.-I.: The latitudinal distributions of auroral zone electric fields and ground magnetic perturbations and their response to variations in the interplanetary magnetic field. J. Geophys. Res. **83**, 2071–2084, 1978b

Jones, R.A., Rees, M.H.: Time dependent studies of the aurora – I. Ion density and composition. Planet. Space Sci. **21**, 537–557, 1973

Küppers, F., Untiedt, J., Baumjohann, W., Lange, K., Jones, A.G.: A two-dimensional magnetometer array for ground-based observations of auroral zone electric currents during the International Magnetospheric Study (IMS). J. Geophys. **46**, 429–450, 1979

Maurer, H., Theile, B.: Parameters of the auroral electrojet from magnetic variations along a meridian. J. Geophys. **44**, 415–426, 1978

Primdahl, F., Walker, J.K., Spangslev, F., Olesen, J.K., Fahleson, U., Ungstrup, E.: Sunlit cleft and polar cap ionospheric currents determined from rocket-borne magnetic field, plasma, and electric field observations. J. Geophys. Res. **84**, 6458–6470, 1979

Rees, M.H.: Auroral ionization and excitation by incident energetic electrons. Planet. Space Sci. **11**, 1209–1218, 1963

Rees, M.H., Romick, G.J., Anderson, H.R., Casserly, R.T.: Calculation of auroral emissions from measured electron precipitation: Comparison with observations. J. Geophys. Res. **81**, 5091–5096, 1976

Rishbeth, H., Garriott, O.K.: Introduction to ionospheric physics. New York, London: Academic Press 1969

Sharp, R.D., Shelley, E.G., Rostoker, G.: A relationship between synchronous altitude electron fluxes and the auroral electrojet. J. Geophys. Res. **80**, 2319–2324, 1975

Wedde, T., Doupnik, J.R., Banks, P.M.: Chatanika observations of the latitudinal structure of electric fields and particle precipitation on November 21, 1975, J. Geophys. Res. **82**, 2743–2751, 1977

Wilhelm, K.: Study of magnetospheric substorm events. In: The Fifth ESA Symp. on European Rocket and Balloon Programmes and on Related Research, Bournemouth, 14–18 April 1980, ESA Special Publication, 1980

Winningham, J.D., Yasuhara, F., Akasofu, S.-I., Heikkila, W.J.: The latitudinal morphology of 10 eV to 10 keV electron fluxes during magnetically quiet and disturbed times in the 2100–0300 MLT sector. J. Geophys. Res. **80**, 3148–3171, 1975

Received June 27, 1980; Revised Version August 6, 1980
Accepted August 7, 1980